

Numerical simulation of the Innoslab laser amplifier based on Yb:YAG crystal

Xiang-Yu Qiao(乔向宇), Qi Liu(刘齐), Xiao-Wei Xing(邢笑伟), Yang-Tian Liu(刘扬天), Rui-Qi Liu(刘瑞琪), Xi-Wei Huang(黄玺玮), Hao-Yu Wang(王浩宇), and Wen-Jun Liu(刘文军)

Citation: Chin. Phys. B, 2026, 35 (**5**): 054205. DOI: 10.1088/1674-1056/ae5175
http://cpb.iphy.ac.cn; http://iopscience.iop.org/cpb

What follows is a list of articles you may be interested in

Breathing dynamics of dissipative pure quartic soliton molecules via spectral filtering effects

Chun-Ting Liu(刘春廷), Jun-You Lu(卢俊佑), Han-Yang Shen(申翰阳), and Zu-Xing Zhang(张祖兴)
Chin. Phys. B, 2026, 35 (**3**): 034205. DOI: 10.1088/1674-1056/adf1eb

Chaotic dynamics of Pr^{3+}/Yb^{3+}-doped all-fiber up-conversion visible fiber laser

Yisong Li(李义松), Yueling Hao(郝悦伶), Juanfen Wang(王娟芬), Xiaohui Chen(陈晓晖), Shengxiang Chen(陈胜祥), Chao Zhou(周超), and Lingzhen Yang(杨玲珍)
Chin. Phys. B, 2026, 35 (**1**): 014208. DOI: 10.1088/1674-1056/ade4b5

A 61-mJ, 1-kHz cryogenic Yb: YAG laser amplifier

Huijun He(何会军), Jun Yu(余军), Wentao Zhu(朱文涛), Qingdian Lin(林庆典), Xiaoyang Guo(郭晓杨), Cangtao Zhou(周沧涛), and Shuangchen Ruan(阮双琛)
Chin. Phys. B, 2021, 30 (**12**): 124206. DOI: 10.1088/1674-1056/ac140d

All-fiber laser seeded femtosecond Yb:KGW solid state regenerative amplifier

Renchong Lv(吕仁冲), Hao Teng(滕浩), Jiajun Song(宋贾俊), Renzhu Kang(康仁铸), Jiangfeng Zhu(朱江峰), and Zhiyi Wei(魏志义)
Chin. Phys. B, 2021, 30 (**9**): 094206. DOI: 10.1088/1674-1056/ac11d3

Spatial chirp in Ti:sapphire multipass amplifier

Wenkai Li(黎文开), Jun Lu(陆俊), Yanyan Li(李妍妍), Xiaoyang Guo(郭晓杨), Fenxiang Wu(吴分翔), Linpeng Yu(於林鹏), Pengfei Wang(王朋飞), Yi Xu(许毅), Yuxin Leng(冷雨欣)
Chin. Phys. B, 2017, 26 (**3**): 034206. DOI: 10.1088/1674-1056/26/3/034206

Numerical simulation of the Innoslab laser amplifier based on Yb:YAG crystal

Xiang-Yu Qiao(乔向宇), Qi Liu(刘齐), Xiao-Wei Xing(邢笑伟), Yang-Tian Liu(刘扬天), Rui-Qi Liu(刘瑞琪), Xi-Wei Huang(黄玺玮), Hao-Yu Wang(王浩宇), and Wen-Jun Liu(刘文军)[†]

School of Physical Science and Technology, Beijing University of Posts and Telecommunications, Beijing 100876, *China*

(Received 6 February 2026; revised manuscript received 5 March 2026; accepted manuscript online 13 March 2026)

A numerical simulation model is developed for a Yb:YAG Innoslab amplifier. By unfolding the multi-pass folded optical path into a one-dimensional slicing model, the model employs differential iterative calculations. This approach enables high-precision characterization of key physical processes, including spot size evolution, pump-laser saturated absorption distribution, the Yb:YAG reabsorption effect, and the spatial dynamic coupling between the pump and seed beams. Notably, a novel correction mechanism for the small-signal gain coefficient in the overlap regions of adjacent passes is proposed for the first time, specifically addressing the energy re-extraction issue neglected in previous models. This correction significantly enhances the computational accuracy and physical fidelity of the model. Validations against existing experimental data demonstrate high consistency between simulated and measured results, confirming the model's excellent applicability and reliability. This work provides a reliable theoretical basis for the structural optimization and parameter tuning of Innoslab amplifiers.

Keywords: Innoslab amplifier, Yb:YAG crystal, Frantz–Nodvik equation, multi-pass amplification

PACS: 42.65.Sf, 42.55.Xi, 42.60.–v

DOI: 10.1088/1674-1056/ae5175 **CSTR:** 32038.14.CPB.ae5175

1. Introduction

Laser systems are evolving toward higher pulse energy, improved beam quality, and shorter pulse widths as ultrashort pulse laser technology advances.[1–17] High-power ultrafast pulse lasers are crucial for a number of applications, including ultrafast scientific research,[18,19] medical diagnosis and treatment,[20] and industrial precision machining.[21,22] The ascendancy of ultrafast solid-state lasers as the mainstream approach stems from their unique combination of high efficiency, high peak power, operational robustness, and cost effectiveness — a set of advantages that make them ideal for a wide range of applications. They can be broadly divided into three categories according to their gain medium architecture: rod,[23–25] thin-disk,[26] and slab.[27–29] Among these, the Innoslab scheme facilitates system integration by providing a more straightforward optical path in contrast to the intricate optical paths of the thin-disk architecture. It supports kilowatt-level power production while maintaining high beam quality and offers efficient conductive cooling compared to the rod construction, effectively minimizing thermal lensing effects and thermally induced birefringence. As such, the Innoslab architecture exhibits exceptional adaptability and versatility in high-power, high-beam-quality laser applications.

Since its introduction by Du *et al.*[30] in 1998, the Innoslab laser amplification technique has achieved a series of significant advances in both experimental research and engineering applications.[31–33] However, because of its unique architecture, relevant theoretical modeling and numerical simulation studies remain relatively scarce, which to some extent restricts its optimization and design. By developing a one-dimensional unfolded model in 2022 for the first time and calculating the output power characteristics of an Nd:YVO_4-based amplifier, Shi *et al.*[34] made a significant contribution to theoretical modeling of Innoslab amplifiers. However, the process of energy re-extraction by the seed beam in the overlap regions was not considered in their calculations.

The main challenges in theoretically modeling this amplification scheme are outlined below. Firstly, while the pump beam enters from the end face, the seed beam propagates inside the gain medium in a folded, multi-pass manner. The conventional Frantz–Nodvik (FN) equation, which assumes straight-through optical paths, cannot accurately capture this asymmetric gain coupling, thus requiring an asymmetric transport model. Secondly, the spot size of the seed beam changes continuously during propagation, causing the spatial overlap between the seed and the pump to vary dynamically along the path. The typical assumption of uniform coupling therefore introduces considerable inaccuracy. Thirdly, the absorption coefficient of the gain medium for the pump beam varies nonlinearly along the pump direction, necessitating a spatially resolved absorption model. Fourthly, in quasi-three-level gain media such as Yb:YAG, the reabsorption effect contributes a non-negligible loss to the output power, which must be included in simulations. Finally, the folded seed beam

[†]Corresponding author. E-mail: jungliu@bupt.edu.cn

© 2026 Chinese Physical Society and IOP Publishing Ltd. All rights, including for text and data mining, AI training, and similar technologies, are reserved.

paths overlap inside the gain medium, leading to energy re-extraction in these regions; ignoring this effect would produce simulation results exceeding actual values.

To address the aforementioned modeling challenges, this work adopts Yb:YAG as the gain medium and unfolds the multi-pass folded optical path of the Innoslab amplifier into a one-dimensional slicing model. Spatially resolved simulations of the energy gain, absorption coefficient, and beam spot size are obtained through differential iterative calculations. The self-reproducing spot evolution caused by thermal lensing, the pump beam's saturated absorption distribution, the reabsorption loss in Yb:YAG, and the dynamic mode matching between the pump and seed beams are all fully included in the model. Compared with existing models, this study introduces for the first time a correction to the small-signal gain coefficient for the overlap regions between adjacent passes of the seed beam in the FN equation, accurately describing the energy re-extraction process in these regions. Using the revised model, the output power characteristics under different conditions were calculated. Comparison with reported experimental data shows good agreement between the simulated and measured results, validating the applicability and accuracy of the proposed theoretical model.

2. Methods

The main components of an Innoslab amplifier are a gain medium, an amplification cavity, a beam-shaping system, a pump source, and a seed source. Its core working principle is that the pump beam injects energy into the gain medium, while the seed beam undergoes multiple passes through the pumped region to realize power amplification. Figure 1(a) provides a schematic representation of the optical arrangement. To guarantee adequate spatial overlap within the gain medium and enable effective energy extraction, the beam profiles of the pump and the seed are separately shaped in the slow axis (X-axis) and the fast axis (Y-axis), respectively.

The filling of the pump region by the seed beam must be maximized in the slow axis. As shown in Fig. 1(b), this maximum filling factor can be achieved by either increasing the number of seed beam passes or expanding the seed beam size. Here, the beam size is determined by the beam shaping before injection into the amplifier and the radius of curvature of the cavity mirrors, while the number of seed beam passes is regulated by the cavity mirror angles and the angle of the seed beam with respect to the Z-axis. The simulations and findings for each of these approaches to improving the seed beam filling factor are presented and discussed later in this work.

In the fast axis, the size of the pump beam must be designed according to the available pump power to ensure its intensity exceeds the saturation intensity (28 kW·cm^{-2}),[32,35] thereby achieving high amplification efficiency. In this axis, the size of the seed beam must match the fundamental mode of the stable resonator formed by the thermal lens and the cavity mirrors. Consequently, the seed beam's spot size in this direction undergoes periodic divergence and convergence according to the cavity mode, forming a self-reproducing pattern, as shown in Fig. 1(c). It is precisely this mechanism that allows the seed beam to propagate back and forth within the gain medium, enabling efficient multi-pass energy extraction.

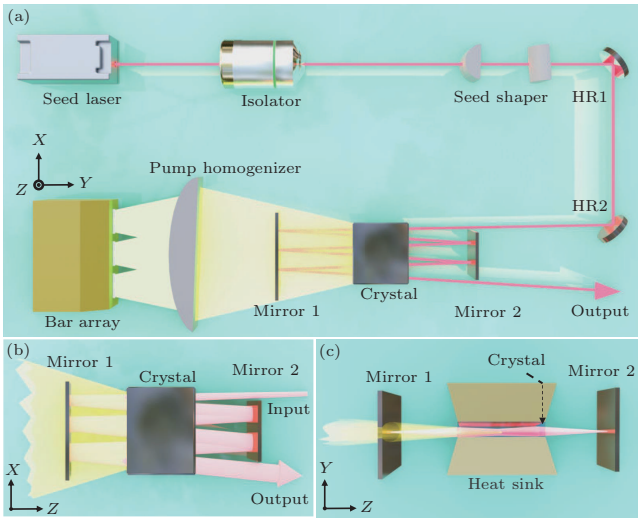


Fig. 1. Schematic diagram of the Innoslab amplifier optical path. HR: high reflector mirror. (a) Overall optical arrangement. (b) Beam path in the slow axis. (c) Beam path in the fast axis.

The aforementioned Innoslab amplifier is modeled mathematically. The center of the pump incident end face of the gain medium is set as the origin of the coordinate system. The geometric dimensions of the gain medium along the X-, Y-, and Z-axes are denoted as W, H, and L, respectively, as illustrated in Fig. 2(a). The optical path is discretized into a series of slices along the propagation direction, each with a width of D_z, as illustrated in Fig. 2(b). D_z is much smaller than the cavity length, and the spatial variation of all relevant parameters within a single slice is assumed to be negligible. The multi-pass folded seed beam is unfolded along the Z-axis into a one-dimensional straight optical path. The seed beam propagates in air at an angle α relative to the Z-axis; upon entering the crystal, this angle changes to β according to the law of refraction. For single-side pumping, following the one-dimensional unfolding of the seed beam, a sign reversal term $P(z^{\pm})$ is introduced to distinguish the direction of the pump, as shown in Fig. 2(c). In the case of dual-end pumping, no directional sign is needed, but the energy contributions from both pump beams at each slice must be summed.[36]

The FN equation,[37] which describes pulse propagation in gain media and was originally derived in 1963, is incorporated into the present model as follows:

$$J_{\text{out}} = J_{\text{sat}} \ln\left\{1 + \left[\exp\left(\frac{J_{\text{in}}}{J_{\text{sat}}}\right) - 1\right] \times \exp\left(g_0 \cdot L_0\right)\right\}, \quad (1)$$

where J_{in} is the input fluence, J_{out} is the output fluence, $J_{\text{sat}} = h\nu/\sigma$ is the saturation fluence, h is Planck's constant, ν is the laser frequency, σ is the stimulated emission cross-section, g_0 is the small-signal gain coefficient, and L_0 is the beam propagation distance. Per-slice output fluence is calculated via the FN equation from the injected pump and seed, then fed to the next slice, repeating this process until all slices in a single pass are processed. The final seed output of a complete pass is used as the input for the next amplification pass, repeating the single-pass iteration until all preset passes are completed. Prior to this, the spatial profiles of both the pump and seed beams must be determined.

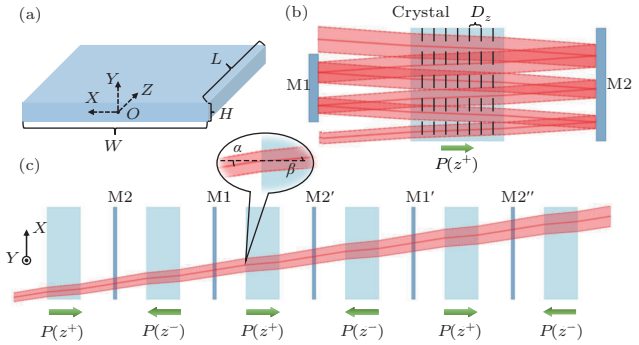


Fig. 2. Schematic diagram of the mathematical model. (a) Crystal dimensions and coordinate system. (b) Six-pass folded beam path. (c) One-dimensional unfolded six-pass beam path.

The pump beam is shaped into a uniform rectangular line-focus spot with its beam waist at the center of the crystal. The pump beam radius in the fast-axis direction, denoted as $w_{\text{py}}(k)$, varies with the propagation distance according to the Gaussian beam propagation formula

$$w_{\text{py}}(k) = \sqrt{w_{\text{py0}}^2 + \left[(k \cdot D_z - z_{\text{py0}}) \cdot \theta_{\text{py}}\right]^2}, \tag{2}$$

where k is the slice index ($0 \le k \le L/D_z$), w_{py0} is the beam waist radius of the pump in the fast axis, z_{py0} is the Z-axis position of the pump waist, and θ_{py} is the divergence angle of the pump beam in the fast axis. In the slow axis, the pump profile follows a super-Gaussian distribution, with its beam radius kept nearly constant over the slices and denoted as w_{px}. The normalized intensity distribution of the pump beam within each slice is given by

$$I_{\text{p}}(x,y,k) = I_{\text{p0}}(k)\frac{\sqrt{2\pi}}{\pi C w_{\text{px}} w_{\text{py}}(k)} \times \exp\left\{-2\left(\frac{2x}{w_{\text{px}}}\right)^{\text{SG}} - 2\left[\frac{y}{w_{\text{py}}(k)}\right]^2\right\}, \tag{3}$$

where $I_{\text{p0}}(k)$ is the central peak intensity of the pump beam in the kth slice, SG is the super-Gaussian order, and $C = 2^{(1-1/\text{SG})} \cdot \Gamma(1+1/\text{SG})$ is the normalization constant, with Γ representing the Gamma function.

The seed beam size in the slow axis at the nth pass and the kth slice can be expressed as

$$w_{\text{lx}}(n,k) = w_{\text{lx0}}\left\{1 + \left[\frac{M_{\text{l}}^2\lambda_{\text{l}}}{\pi w_{\text{lx0}}^2}\left(k\frac{D_z}{n_{\text{l}}\cos(\beta)} + \frac{nL}{n_{\text{l}}\cos(\beta)} + \frac{2nD}{\cos(\alpha)} - \frac{z_{\text{lx0}}}{\cos(\alpha)}\right)\right]^2\right\}^{1/2}, \tag{4}$$

where w_{lx0} is the waist radius of the seed beam in the slow axis, z_{lx0} is the Z-axis position of the seed waist, M_{l}^2 is the beam quality factor of the seed beam, λ_{l} is the seed wavelength, n_{l} is the refractive index of the gain medium at the seed wavelength, and D is the distance between the cavity mirror and the crystal surface.

Owing to self-reproducing spot evolution in the fast axis, the spot radius of the seed beam in this direction remains unchanged across different passes for a given slice index k. Before reaching the position of the thermal lens, the fast-axis spot radius of the seed beam is expressed as

$$w_{\text{ly}}(k) = w_{\text{ly0}}\left\{1 + \left[\frac{M_{\text{l}}^2\lambda_{\text{l}}}{\pi w_{\text{ly0}}^2}\left(k\frac{D_z}{n_{\text{l}}\cos(\beta)} - \frac{z_{\text{ly0}}}{\cos(\alpha)}\right)\right]^2\right\}^{1/2}, \tag{5}$$

where w_{ly0} is the waist radius of the seed beam in the fast axis, and z_{ly0} is the Z-axis position of the seed waist. Under the pump beam, the focal length of the cylindrical thermal lens induced in the gain medium can be approximated as

$$f_{\text{th}} = \frac{\lambda \cdot b \cdot 2w_{\text{py}}}{\chi \cdot \eta_{\text{h}} \cdot P_{\text{abs}}},$$

where b is the width of the pump beam along the slow axis, and P_{abs} is the absorbed pump power. For Yb:YAG crystal: $\chi = 10^{-5}$ K^{-1} (thermo-optic coefficient),[38] $\lambda = 8.6$ W·m^{-1}·K^{-1} (thermal conductivity),[39] and $\eta_{\text{h}} = 0.1$ (fractional thermal load).[40] Since the heat generated by the pump beam is concentrated mainly near the irradiated end face of the crystal, the thermal lens is approximated to be located at the pump incident end face of the gain medium.[41] After the seed beam passes through the thermal lens, its fast-axis spot radius in subsequent propagation must be recalculated according to the new focusing condition.

Once the spot size of the seed beam at each slice is obtained, its normalized intensity distribution is given by

$$I_{\text{l}}(x,y,n,k) = I_{\text{l0}}(n,k)\frac{2}{\pi w_{\text{lx}}(n,k) w_{\text{ly}}(n,k)} \times \exp\left[-\frac{2x^2}{w_{\text{lx}}(n,k)^2} - \frac{2y^2}{w_{\text{ly}}(k)^2}\right], \tag{6}$$

where $I_{\text{l0}}(n,k)$ is the central peak intensity of the seed beam.

The spatial overlap between the pump beam and the seed beam directly determines the energy conversion efficiency.

This is quantified by the pump-seed overlap integral γ, defined as

$$\gamma(n,k)=\frac{\iint I_{\mathrm{p}}(x,y,k)I_{\mathrm{l}}(x,y,n,k)\,\mathrm{d}x\mathrm{d}y}{\sqrt{\iint I_{\mathrm{p}}^2(x,y,k)\,\mathrm{d}x\mathrm{d}y\cdot\iint I_{\mathrm{l}}^2(x,y,n,k)\,\mathrm{d}x\mathrm{d}y}}. \quad (7)$$

The pump-seed overlap integral γ ranges from 0 to 1. A value closer to 1 indicates better spatial matching between the pump and the seed. This integral accounts for the fact that the spot sizes of the pump and seed may not be perfectly equal at every slice, ensuring that only effectively coupled energy is considered.

Having characterized the spatial distributions of the pump and seed, the evolution of laser energy within each slice is described. Under steady-state laser amplification, the population densities of the upper level $^2\mathrm{F}_{5/2}(N_2)$ and the lower level $^2\mathrm{F}_{7/2}(N_1)$ in each slice satisfy the following rate equations:

$$\begin{cases}\dfrac{\sigma_{\mathrm{ap}}I_{\mathrm{p}}}{h\nu_{\mathrm{p}}}N_1-\dfrac{\sigma_{\mathrm{ep}}I_{\mathrm{p}}}{h\nu_{\mathrm{p}}}N_2-\dfrac{N_2}{\tau}-\dfrac{\sigma_{\mathrm{el}}I_{\mathrm{l}}}{h\nu_{\mathrm{l}}}N_2+\dfrac{\sigma_{\mathrm{al}}I_{\mathrm{l}}}{h\nu_{\mathrm{l}}}N_1=0,\\ N_1+N_2=N_{\mathrm{Yb}},\end{cases} \quad (8)$$

where σ_{ap} is the absorption cross-section of the pump beam, σ_{ep} is the emission cross-section of the pump beam, ν_{p} is the pump frequency, ν_{l} is the seed frequency, and τ is the fluorescence lifetime of the upper laser level. The second equation ensures population conservation, with N_{Yb} representing the Yb^{3+} ion population density in the Yb:YAG gain medium.

Given the population inversion density at each slice, the pump beam attenuation coefficient $\alpha_{\mathrm{p}}(n,k)$ and the small-signal gain coefficient $g(n,k)$ at the corresponding slice can be calculated. The pump power decays exponentially along the propagation direction. The pump power at the $(k+1)$th slice is expressed in terms of the attenuated pump power at the kth slice as

$$P_{n,k+1}=P_{n,k}\exp[-\alpha_{\mathrm{p}}(n,k)D_z]. \quad (9)$$

The attenuation coefficient is given by

$$\alpha_{\mathrm{p}}(n,k)=\sigma_{\mathrm{ap}}N_1(n,k)-\sigma_{\mathrm{ep}}N_2(n,k). \quad (10)$$

In each slice, within regions where adjacent passes (the nth and $(n+1)$th) of the seed beam do not overlap, the small-signal gain coefficient is

$$g_{\text{non-overlap}}(n,k)=\sigma_{\mathrm{el}}\left[N_2(n,k)-\frac{\sigma_{\mathrm{al}}}{\sigma_{\mathrm{el}}}N_1(n,k)\right]. \quad (11)$$

When adjacent passes of the seed beam overlap, the small-signal gain coefficient for the $(n+1)$th pass in the overlap region is

$$g_{\mathrm{overlap}}(n+1,k)=\sigma_{\mathrm{el}}N_{\mathrm{rem}}(n,k)-\sigma_{\mathrm{al}}\left[N_{\mathrm{Yb}}-N_{\mathrm{rem}}(n,k)\right]. \quad (12)$$

The residual population inversion density N_{rem} after energy extraction by the nth pass in the overlap region is calculated from the FN equation as

$$N_{\mathrm{rem}}(n,k)=\frac{N_2-N_1}{1+[\exp(J_{\mathrm{in}}/J_{\mathrm{sat}})-1]\exp(g_{\text{non-overlap}})}. \quad (13)$$

A two-dimensional elliptical Gaussian overlap factor ξ is introduced to describe the spatial matching of adjacent seed passes, defined as

$$\xi_{n+1,k'}=\frac{2w_{\mathrm{lx}}(n,k)w_{\mathrm{lx}}(n+1,k')}{w_{\mathrm{lx}}^2(n,k)+w_{\mathrm{lx}}^2(n+1,k')}\times\exp\left[-\frac{2\Delta x^2}{w_{\mathrm{lx}}^2(n,k)+w_{\mathrm{lx}}^2(n+1,k')}-\frac{\Delta y^2}{w_{\mathrm{ly}}^2(n,k)}\right], \quad (14)$$

where Δx and Δy are the center-to-center separations of the two beams along the X- and Y-axes. This overlap factor quantifies the intensity-weighted spatial overlap of the elliptical Gaussian beams.

The effective small-signal gain coefficient for the $(n+1)$th pass at the kth slice is expressed as

$$g_{\mathrm{eff}}(n+1,k')=\xi\cdot g_{\mathrm{overlap}}(n+1,k')+(1-\xi)\cdot g_{\text{non-overlap}}(n+1,k'). \quad (15)$$

Substituting the corrected small-signal gain coefficient into Eq. (1) yields the output fluence

$$J_{\mathrm{out}}(n+1,k')=J_{\mathrm{sat}}\ln\left\{1+\left[\exp\left(\frac{J_{\mathrm{in}}(n+1,k')}{J_{\mathrm{sat}}}\right)-1\right]\times\exp\left[g_{\mathrm{eff}}(n+1,k')\cdot L_{\mathrm{eff}}\right]\right\}, \quad (16)$$

where $L_{\mathrm{eff}}=n_1D_z/\cos(\beta)$ is the effective optical path length, and $J_{\mathrm{sat}}=h\nu/(\sigma_{\mathrm{el}}+\sigma_{\mathrm{al}})$ is the saturation fluence accounting for reabsorption.

This model extends the standard FN equation by incorporating energy re-extraction in overlap regions of the seed beam paths. It does not include corrections for possible parasitic oscillations within the cavity. Given the amplifier injection conditions, the output power characteristics can be numerically simulated via iterative calculations based on the above model and formulas.

3. Results and discussion

To validate the rationality of the established model, the experimental parameters from Russbüldt *et al.*[31] are first adopted as model I. In that experiment, a Yb:YAG crystal with a doping concentration of 2.5 at.% was used as the gain medium, dual-end pumped at a total power of 1250 W. The seed beam had an average power of 2.3 W, a central wavelength of 1030 nm, and a repetition rate of 20 MHz. The amplifier was configured as a seven-pass Innoslab amplifier with a cavity length of 35 mm. The cavity mirrors were cylindrical concave and convex mirrors; however, since their curvature was not provided in the reference, under the condition that the seed beam can basically cover the pump region, they are approximated as flat mirrors in the simulation. The emission cross-section, geometric dimensions of the Yb:YAG crystal, and other parameters are listed in Table 1.

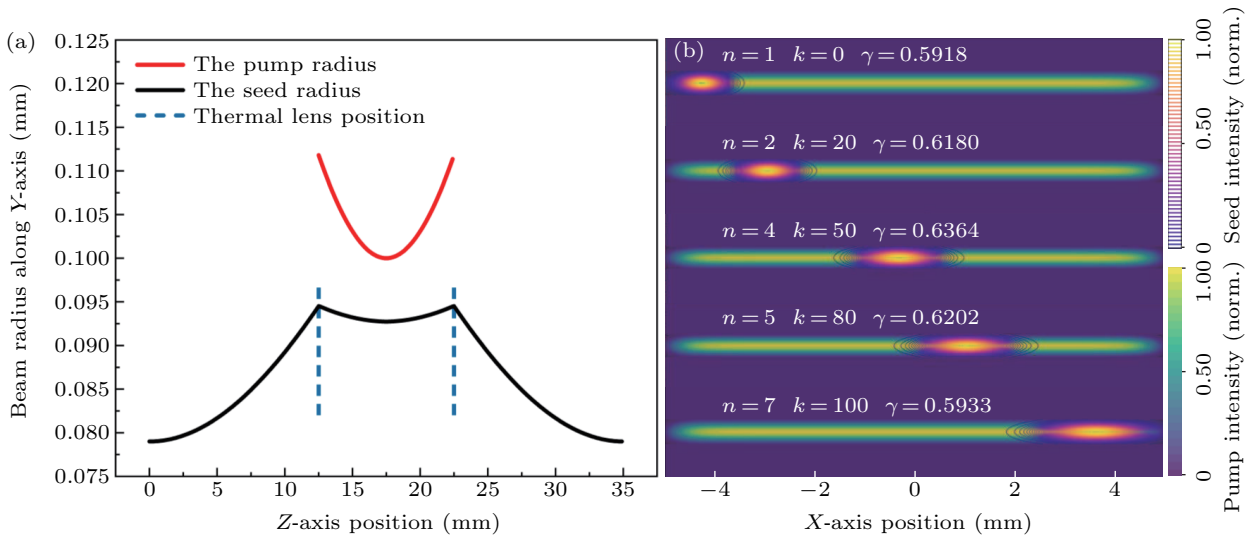


Fig. 3. Spatial distributions of the pump and seed beams. (a) Spot sizes of the pump and seed along the fast axis at different positions. (b) Pump-seed coupling states at different positions.

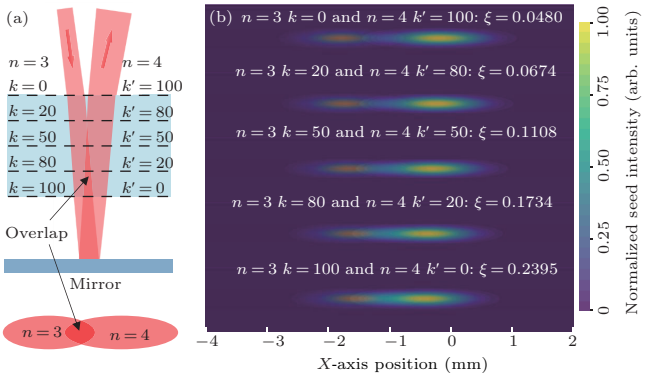


Fig. 4. Schematic representation of the seed overlap in model I. (a) Seed beam paths for the 3rd and 4th passes. (b) Spatial distributions of the seed beams for the 3rd and 4th passes.

Table 1. Parameter values used in the model.

Parameter	Value	Parameter	Value
λ_l (nm)	1030	λ_p (nm)	940
W (mm)	10	w_{py0} (mm)	0.1
H (mm)	1	w_{px} (mm)	5
L (mm)	10	z_{py0} (mm)	5
D_z (mm)	0.1	Model I: α (rad)	0.042
SG	20	Model II: α (rad)	0.025
θ_{py} (rad)	0.1	Model I: N_{yb} (mm^{-3})	3.48×10^{17}
n_l	1.82	Model II: N_{yb} (mm^{-3})	2.78×10^{17}
σ_{el} (mm^2)[42]	2.0×10^{-18}	σ_{ap} (mm^2)[42]	0.1×10^{-18}
σ_{ep} (mm^2)[42]	0.2×10^{-18}	σ_{al} (mm^2)[42]	0.8×10^{-18}
M_l^2	1.2	τ (s)[42]	950×10^{-6}

The spot sizes of the pump and seed beams along the fast axis at different positions on the Z-axis are shown in Fig. 3(a). In the fast axis, the pump beam is focused at the center of the gain medium, while the seed beam is focused at $z_{ly0} = -12.5$ mm with a beam waist radius of $w_{ly0} = 0.079$ mm. The spot sizes and spatial distributions of the pump and seed at different positions directly determine the calculation of the pump-seed overlap integral γ. Figure 3(b) presents the spatial intensity profiles of the two beams and the corresponding calculated overlap integral at several representative positions. Analysis indicates that, since the pump beam is always wider than the seed beam in the slow axis, the primary factor affecting the overlap integral is their relative spatial distributions in the fast axis.

In the slow axis, the seed beam is focused at $z_{lx0} = -170$ mm with a beam waist radius of $w_{lx0} = 0.15$ mm. Through the folded seven-pass configuration between the two cavity mirrors, the seed beam essentially covers the entire pumped region. While achieving high coverage of the pumped region, spatial overlap between adjacent passes of the seed beam within the gain medium is inevitable. Taking the spatial distributions of the 3rd and 4th passes as an example (Fig. 4(a)), their overlap region is where energy re-extraction occurs. Due to the finite angle between the 3rd and 4th passes, the area of overlap at each slice gradually decreases as the slice index k increases, as presented in Fig. 4(b).

As shown in Fig. 5(a), the output power characteristics of the amplifier under the specified parameters were simulated. Two curves are presented: one neglecting the overlap-region energy re-extraction (dashed curve, using $g_{\text{non-overlap}}$), and one incorporating the overlap-region correction (solid curve, using g_{eff}). The results demonstrate that including the corrected small-signal gain coefficient yields better agreement with experimental measurements. In the linear power amplification regime (total pump power from 600 W to 1250 W), 10 evenly spaced data points were selected for systematic error analysis. The average relative error between simulation and experiment is only 1.34%, indicating excellent quantitative agreement. Although the simulation simplified the cavity mirrors as flat, potentially affecting the overlap condition of the seed beam, the overall agreement remains reasonable, since the seed beam essentially covers the pumped region. This further validates the rationale of applying the small-signal gain correction.

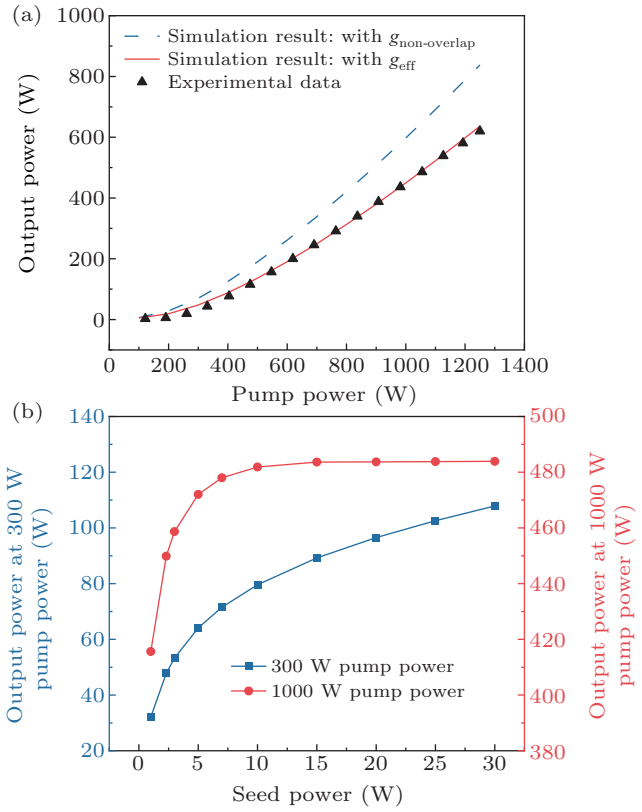


Fig. 5. Calculated output power results for model I. (a) Comparison between simulated and experimentally measured output power. (b) Output power under different seed beam input levels.

Next, the effect of seed injection power on output power was analyzed with other parameters fixed. Simulations were conducted for pump powers of 300 W and 1000 W, as shown in Fig. 5(b). The results indicate that once the seed power reaches a certain level, the extractable energy in the gain medium approaches depletion. Beyond this point, increasing seed power does not yield additional amplification. Higher seed power promotes more efficient energy extraction, and at higher pump powers, the seed reaches the saturation level more rapidly, driving the amplifier into the gain-saturation regime, where the output power remains essentially constant with increasing seed power.

To further investigate the impact of seed beam shaping, simulations were performed for different numbers of passes and filling factors. Figure 6(a) compares the output power for 3pass, 5pass, and 7pass configurations at various pump powers, assuming maximal seed coverage of the pumped region. Figure 6(b) illustrates the corresponding optical paths. The results indicate that, for a given filling factor, more passes provide higher cumulative gain, favoring higher output power. In practice, however, increasing passes reduces the inter-mirror angle and increases the risk of parasitic oscillations, while heat accumulation becomes more significant, limiting further efficiency gains.

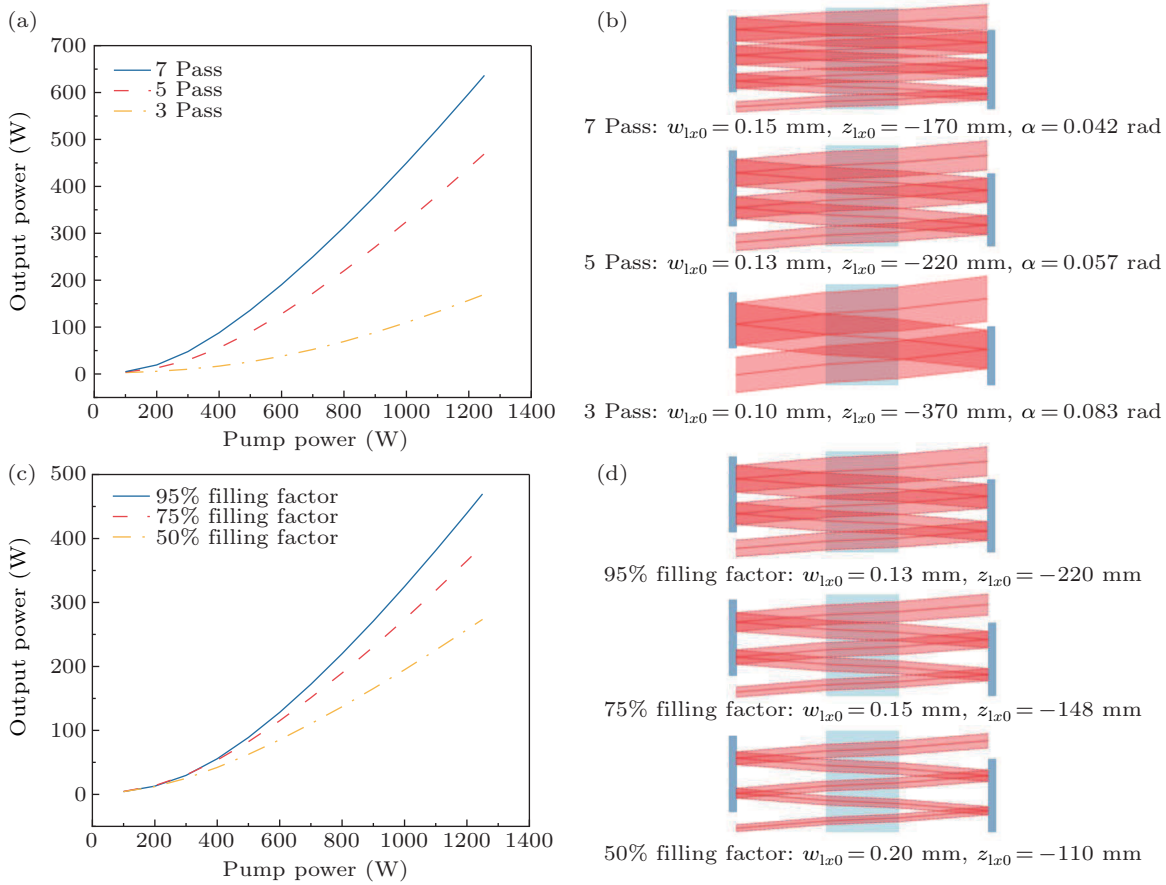


Fig. 6. Amplifier output power under different seed beam shaping parameters. (a) Output power under different pass numbers. (b) Schematic of seed beam with different pass numbers. (c) Output power under different filling factor. (d) Schematic of seed beam with different filling factor.

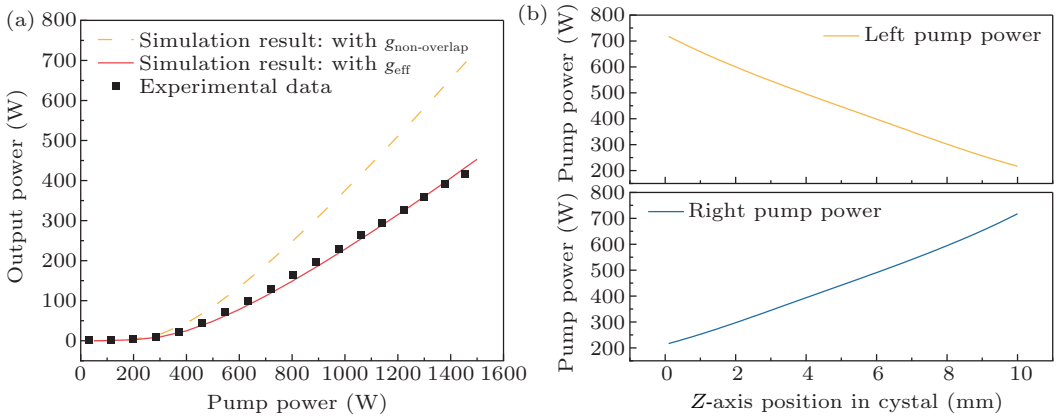


Fig. 7. Calculation results of output power under the parameters of model II. (a) Comparison between simulations and experimental values of output power. (b) Pump power at different positions along the Z-axis in the crystal.

The influence of seed beam filling factor was examined in a 5pass configuration. Figure 6(c) shows output power for different filling factors, with the corresponding optical paths in Fig. 6(d). The results demonstrate that seed beam coverage of the pumped region is a critical factor determining energy extraction efficiency and output power. In amplifier design, either the divergence properties of the Gaussian beam should be exploited, or a hybrid cavity with cylindrical mirrors should be employed to maximize coverage and energy extraction.

Finally, model II, based on the experiment by Liang *et al.*,[33] was simulated. This setup used a 2 at.% Yb:YAG crystal, with a 10 W seed at 1030 nm and 175 kHz in a nine-pass configuration. All other parameters match Table 1, with a cavity length of 45 mm, consisting of one flat and one cylindrical mirror ($R = -700$ mm). In the simulation, concave lenses with $f = -350$ mm were inserted at the end of the 2nd, 4th, 6th, and 8th passes to emulate the cylindrical mirror shaping. The seed beam parameters were $w_{\text{ly0}} = 78$ μm, $z_{\text{ly0}} = -17.5$ mm, $w_{\text{lx0}} = 200$ μm, $z_{\text{lx0}} = -80$ mm. The 9pass output beam diameter of 4 mm matched experimental values. Comparing simulations with and without the overlap-region correction (Fig. 7(a)), the corrected small-signal gain coefficient showed better agreement with the experiment. In the linear amplification regime (800–1400 W pump power), the average relative error across eight evenly spaced data points is only 3.45%, confirming excellent quantitative agreement.

Using the parameters of model II and based on the established model, the pump power distribution at different positions along the pump direction in the gain medium was calculated (Fig. 7(b)). The model assumes that the dual-end pump beams achieve good spatial overlap inside the gain medium and that the absorption of the pump beam by the medium is uniform. The calculated overall absorption of the pump beam by the gain medium is about 70.1%, which closely matches the experimentally measured value of approximately 73.0% reported in Ref. [33], thereby further validating the effectiveness of the model.

4. Conclusion

This study establishes a high-precision numerical model for Yb:YAG Innoslab amplifiers, which unfolds the folded multi-pass optical path into a one-dimensional segmented structure to simulate asymmetric gain coupling via differential iterative calculations. Key physical processes such as the thermal lens, gain saturation, reabsorption loss, and dynamic pump–seed spatial coupling are fully incorporated in the model. For the first time, this work proposes a correction mechanism for the small-signal gain coefficient in the overlap region between adjacent seed passes, accurately describing the energy re-extraction in this region.

The model provides reliable theoretical support for the design optimization and parameter tuning of higher-power, higher-efficiency Innoslab amplifiers, facilitating their application in related fields. With adjusted rate equations and optical parameters, the established model is applicable to numerical simulations of other gain media, such as Nd:YVO_4, Yb:LuAG, etc. In addition, in the practical design of Innoslab amplifiers, with the increase in the number of seed beam passes and output power, adverse effects such as heat accumulation in the gain medium and intracavity parasitic oscillation will be significantly exacerbated. A comprehensive trade-off must be conducted to achieve the optimal design of the amplifier.

Acknowledgments

Project supported by the National Natural Science Foundation of China (Grant No. 10225417) and the National Basic Research Program of China (Grant No. 2006CB601003).

References

[1] Ahamed A, Myat H, Rawat A, McPhillips L N and Islam M S 2026 *Adv. Photon.* **8** 016008
[2] Zou D F, Liu R M, Shi Y Q, Zhang A Y, Li J L, Chen G J, Dang H, Song Y J, Hu M L and Shum P P 2025 *Adv. Photon.* **7** 016005
[3] Zhou Y Y, Wang Y, Zhang K, Leng H Q, Müller-Buschbaum P, Li N and Qiao L 2025 *Opto. Electron. Adv.* **8** 250096

[4] Xing X W, Jiang Y J, Huang X W, Chen W, Wang K J, Zhang Z Y, Liu M W, Huang Z W, Hu Q P, Zhou Q, Han J F, Teng H, Liu W J and Wei Z Y 2025 *Ultrafast Sci.* **5** 0115

[5] Mahmoodpoor A, Alekseev P A, Gasnikova K A, Natalia K, Larin A, Makarov S and Furasova A 2025 *Opto. Electron. Adv.* **8** 250110

[6] Li K, Hu Q P, Chen W, Gao C, Feng H Y, Zhang Z R, Li X, Li Z F and Zhou Q 2025 *Chin. Phys. Lett.* **42** 120407

[7] Huang Z W, Li P B, Xing X W, Liu Q, Wang K J, Liu W J, Teng H, Zhu J F and Wei Z Y 2025 *Chin. Phys. Lett.* **42** 024203

[8] Gu H X, Zhang J M, Chen X W, Yu F H, Xu D Y, Liu S Q, Lin W H, Shi X B, Huang Z X, Yang X J, Hu Q C and Shao L Y 2025 *Opto-Electron. Adv.* **8** 240270

[9] Chen Y F, Ju L B, Wu C N, Yu M Y, Zhang H, Wu S Z and Zhou C T 2025 *Ultrafast Sci.* **5** 0118

[10] Cai J, Shou Y R, Wen H, Han L Q, Gong Z, Tajima T, Yu J Q and Yan X Q 2025 *Ultrafast Sci.* **5** 0116

[11] Ardana-Lamas F, Cousin S L, Lignieres J and Biegert J 2025 *Ultrafast Sci.* **5** 0128

[12] Hu X, Guo J, Hu G W, Yoo S and Tang D Y 2024 *Adv. Photon.* **6** 066005

[13] Xiao Y J, Xing X W, Cui W W, Chen Y Q, Zhou Q and Liu W J 2023 *Chin. Phys. Lett.* **40** 054201

[14] Cui W W, Xing X W, Chen Y Q, Xiao Y J, Ye H and Liu W J 2023 *Chin. Phys. Lett.* **40** 024201

[15] Liu M L, Wu H B, Liu X M, Wang Y R, Lei M, Liu W J, Guo W and Wei Z Y 2021 *Opto-Electron. Adv.* **4** 200029

[16] Liu X M and Cui Y D 2019 *Adv. Photon.* **1** 016003

[17] Xing X W, Han Y C, Huang X W, Chen W, Zhang Z Y, Liu M W, Hu Q P, Hu G J, Xian G Y, Zhou Q, Lin X, Yang H T, Teng H and Liu W J 2025 *Adv. Funct. Mater.* e19204

[18] Zou J H, He H S, Song L M, Huang L, Lan J B, Lan L, Chen T T, Kong C H, Sun Z P and Luo Z Q 2025 *Adv. Photon.* **7** 046009

[19] Zhang X T, Yang C B, Yuan X, Han M H, Cao Z, Peng J B and Yu X 2025 *Chin. Phys. B* **34** 094701

[20] Chen Z, Meng C L, Lin H L, Fixler D and Zhang H 2025 *Adv. Photon. Nexus* **4** 066009

[21] Yin J B, Wu Y L and Hong M H 2025 *Photon. Insights* **4** C06

[22] Li C H, Liang H T, Yang Y, Yu Z Y, Zhang X, Ma X M, Lu W L, Sun Z R and Cheng Y 2022 *Chin. Phys. Lett.* **39** 077901

[23] Lux O, Wernham D, Bravetti P, Mcgoldrick P, Lecrenier O, Riede W, D'Ottavi A, Sanctis V D, Schillinger M, Lochard J, Marshall J, Lemmerz C, Weiler F, Mondin L, Ciapponi A, Kanitz T, Elfving A, Parrinello T and Reitebuch O 2020 *Opt. Lett.* **45** 1443

[24] Shen J P, Chen Y, Chen L, Xing F Y, Zhang F B, Xia R Z, Zuo H Y, Xiong F and Jiang R R 2025 *Chin. Phys. Lett.* **42** 044202

[25] Shen J P, Huang X, Jiang S T, Jiang R R, Wang H Y, Lu P, Xu S C and Jiao M Y 2022 *Chin. Phys. Lett.* **39** 104201

[26] Diebold A, Saltarelli F, Graumann I J, Saraceno C J, Phillips C R and Keller U 2018 *Opt. Express* **26** 012648

[27] Deng B, Zhang H L, XU L, Mao Y F, He J L and Xin J G 2014 *Chin. Phys. Lett.* **31** 114201

[28] Liu L, Zhou S H, Liu Y, Wang Z, Wang G and Zhao H 2017 *Chin. Phys. Lett.* **34** 064202

[29] Yang G D, Meng X H, Bi Y, Mao D, Zhao X L, Gong Z Q, Jiao T M, Yang J, Shao X, Liu H Y, Xu W T, Chen J H and Li P X 2025 *Opt. Lett.* **50** 5430

[30] Du K M, Wu N L, Xu J D, Giesekus J, Loosen P and Poprawe R 1998 *Opt. Lett.* **23** 370

[31] Russbueldt P, Mans T, Weitenberg J, Hoffmann H D and Poprawe R 2010 *Opt. Lett.* **35** 4169

[32] Russbueldt P, Mans T, Rotarius G, Weitenberg J, Hoffmann H D and Poprawe R 2009 *Opt. Express* **17** 12230

[33] Gao Y X, Guo J, Huang Y G, Gao Z C, Gan Z B, Tu Z H, Liang X Y and Li R X 2023 *Opt. Lett.* **48** 5328

[34] Shi B N, Li J T, Ye S, Nie H K, Yang K J, He J L, Li T and Zhang B T 2022 *Opt. Express* **30** 11026

[35] DeLoach L D, Payne S A, Chase L L, Smith L K, Kway W L and Krupke W F 1993 *IEEE J. Quantum Electron.* **29** 1179

[36] Fulford B S 2015 *An Industrial Ultrashort Pulse Thin Slab Laser Amplifier* (Ph.D. Dissertation) (Edinburgh: Heriot-Watt University)

[37] Frantz L M and Nodvik J S 1963 *J. Appl. Phys.* **34** 2346

[38] Aggarwal R L, Ripin D J, Ochoa J R and Fan T Y 2005 *J. Appl. Phys.* **98** 103514

[39] Chénais S, Balembois F, Druon F, Lucas-Leclin G and Georges P 2004 *IEEE J. Quantum Electron.* **40** 1235

[40] Fan T Y 1993 *IEEE J. Quantum Electron.* **29** 1457

[41] Xu L 2015 *LD-pumped Innoslab Laser Oscillators and Amplifiers* (Ph.D. Dissertation) (Beijing: Beijing Institute of Technology) (in Chinese)

[42] Beecher S J, Grant-Jacob J A, Hua P, Prentice J J, Eason R W, Shepherd D P and Mackenzie J I 2017 *Opt. Mater. Express* **7** 1628